A grid of 800 000 models of delta Scuti stars using MESA and GYRE

Simon J. Murphy,[1★] Timothy R. Bedding,[2] and Anuj Gautam[1]
[1] Centre for Astrophysics, University of Southern Queensland, Toowoomba, QLD 4350, Australia
[2] Sydney Institute for Astronomy, School of Physics, University of Sydney NSW 2006, Australia

Accepted XXX. Received YYY; in original form ZZZ

ABSTRACT

The rapidly increasing number of delta Scuti stars with regular patterns among their pulsation frequencies necessitates modelling tools to better understand the observations. Further, with a dozen identified modes per star, there is potential to make meaningful inferences on stellar structure using these young δ Sct stars. We compute and describe a grid of >800,000 stellar models from the early pre-main-sequence to roughly one third of the main-sequence lifetime, and calculate their pulsation frequencies. From these, we also calculate asteroseismic parameters and explore how those parameters change with mass, age, and metal mass fraction. We show that the large frequency separation, $\Delta\nu$, is insensitive to mass at the zero-age main sequence. In the frequency regime observed, the $\Delta\nu$ we measure (from modes with $n \sim 5$–9) differs from the solar scaling relation by ∼13%. We find that the lowest radial order is often poorly modelled, perhaps because our non-rotating models lack the oblateness of real stars. We show an application of the grid to five newly modelled stars, including two pre-main-sequence stars each with 15+ modes identified. We make the grid available as a community resource.

Key words: asteroseismology – stars: evolution – stars: fundamental parameters – stars: pre-main-sequence – stars: variables: δ Scuti

1 INTRODUCTION

The discovery of regularly spaced pulsation frequencies amongst the pressure modes of young intermediate-mass (1.3–2.2 $M_\odot$) stars (Bedding et al. 2020) has ushered in a new era of asteroseismic investigation. The once-thorny mode identification problem (Guzik et al. 2021; Kurtz 2022) is steadily gaining traction for some young delta Scuti stars. Asteroseismic ages from several δ Sct stars in young clusters and/or stellar associations have now been determined (Murphy et al. 2021; Steindl et al. 2022; Kerr et al. 2022a,b; Murphy et al. 2022; Currie et al. 2023; Scutt et al. 2023). The recent discovery of many new δ Sct stars in TESS light curves of the Pleiades (Bedding et al. 2023) suggests that asteroseismic ages may come to sit beside isochrones (e.g. Gagné et al. 2023), kinematics (e.g. Squicciarini et al. 2021; Miret-Roig et al. 2022; Žerjal et al. 2023) and lithium depletion (e.g. Galindo-Guil et al. 2022; Wood et al. 2023) as key methods for dating young clusters.

For solar-like oscillators, that regular frequency spacing is known as the large-frequency separation, $\Delta\nu$, and it scales with the square-root of the mean stellar density, $\Delta\nu \propto \sqrt{\rho}$ (Ulrich 1986; Kjeldsen & Bedding 1995). This has been exploited extensively in the *Kepler* era to characterise red giants (see reviews by Hekker 2020; Basu & Hekker 2020; Jackiewicz 2021) and perform Galactic archaeology (see review by Serenelli et al. 2021). Models have predicted that a similar scaling relation would apply to δ Sct stars (Reese et al. 2008; Suárez et al. 2014). Using eclipsing binaries, García Hernández et al. (2015, 2017) verified that the $\Delta\nu$ determined at low radial orders correlated with stellar density, and that this scaling relation also applies to rotating stars. Mirouh et al. (2019) further demonstrated that even rapid rotators showed regular frequency patterns in their models. This probably explains why Pleiades stars with $v \sin i \sim 200$ km s^{-1} have measurable $\Delta\nu$ (Murphy et al. 2022).

A common approach to asteroseismic modelling is to construct an $n + 1$ dimensional grid of n stellar parameters that describe evolutionary tracks, whose properties are evaluated along the additional time dimension. Such properties include 'classical' observables such as temperature and luminosity, and asteroseismic properties, namely the stellar oscillation frequencies. In this paper we present such a grid, calculated for young δ Sct stars, that has already been used to model various targets (Kerr et al. 2022a,b; Murphy et al. 2022; Currie et al. 2023; Scutt et al. 2023). We also make this grid available as a community resource. We describe the physics and computation of the grid, as well as calculation of the pulsation frequencies, in Sec. 2. We explore various asteroseismic parameters across the grid in Sec. 3, including scaling relations in Sec. 3.2. In Sec. 4 we apply this grid to real stars, including two new pre-main-sequence ('pre-MS') stars that have never been modelled asteroseismically.

★ E-mail: simon.murphy@usq.edu.au (SJM)

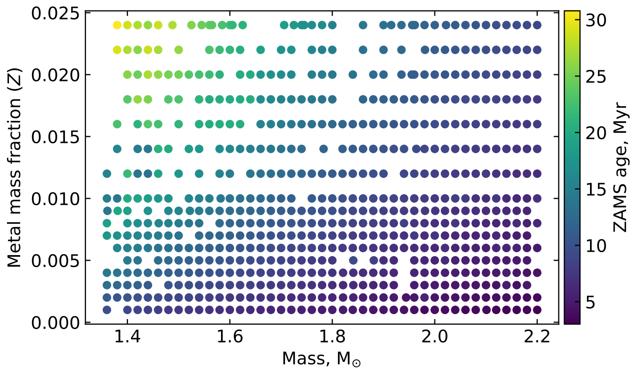

Figure 1. Distribution of tracks across a mass–metallicity grid. Shown in colour is the stellar age at the ZAMS, as defined in Sec. 2.3.

2 MODELLING PARAMETERS

2.1 MESA evolutionary models

Stellar evolutionary models were calculated with MESA r15140 (Paxton et al. 2011, 2013, 2015, 2018, 2019). We calculated pre-MS models using an initial core temperature of 9×10^5 K, which determines age=0 for our models, and evolved them to approximately one third of their MS lifetimes. The independent variables of the models were mass and metallicity; other 'variables' were either dependent or fixed. Neither rotation nor accretion was included in these models.

Models were calculated in a grid that is approximately uniformly spaced in mass, from 1.36 to 2.20 $M_\odot$ at 0.02-$M_\odot$ spacing. Spacing in metallicity is exact, with initial metal mass fractions, Z, between 0.001 and 0.010 at a spacing of 0.001, then spaced by 0.002 from 0.012 to 0.024. However, not all MESA tracks (M–Z pairs) successfully converged. For tracks that did not, the mass was increased by 0.001 $M_\odot$ and the track was retried for up to five iterations before the track was abandoned. Hence, there is some heterogeneity in mass, as shown in Fig. 1. The grid comprises 664 tracks.

2.1.1 Composition and nuclear reactions

The initial abundances were based on Z. While Steindl et al. (2022) showed that helium abundance contributes to the uncertainty in modelling of young δ Sct stars, Murphy et al. (2022) found that the effect on stellar densities is 1–2 orders of magnitude less than that of rotation. Given that our models do not include rotation, we chose not to set the helium abundance as an independent variable in our non-rotating models. Instead, we calculated helium abundances as a function of the stellar metallicity, as follows. For a given track, we first calculated the difference between the stellar metallicity and the solar metallicity, $dZ = Z - Z_\odot$, where for $Z_\odot$ we used the bulk solar metal mass fraction of 0.0142 from Asplund et al. (2009). The helium abundances were then calculated assuming a helium enrichment rate $dY/dZ = 1.4$, which is a relatively poorly constrained quantity in the literature but for which a value of 1.4 appears reasonable (Brogaard et al. 2012; Li et al. 2018; Verma et al. 2019; Lyttle et al. 2021 and references therein). We adopted a helium mass fraction of $Y_\odot = 0.28$ for the Sun, and used our adopted helium enrichment ratio to calculate the stellar helium mass fraction Y:

$$Y = Y_\odot + dZ\frac{dY}{dZ}. \quad (1)$$

The hydrogen mass fraction, X, constitutes the remainder of the initial composition, with

$$X + Y + Z = 1. \quad (2)$$

We included initial quantities of ^{2}H (deuterium) equal to 2×10^{-5} of ^{1}H (Stahler et al. 1980; Linsky 1998), and of ^{3}He equal to 1.66×10^{-4} of ^{4}He. Stellar abundances otherwise followed Asplund et al. (2009), with the corresponding opacity settings. We used the `pp_and_cno_extras` nuclear reaction network with the `jina reaclib` reaction rates.

2.1.2 Mixing, convection, and atmospheres

Stars are fully convective for part of the pre-MS stage, hence have a uniform composition to which different mixing parameters make little difference. Perhaps for this reason, Murphy et al. (2021) found that the chosen value of $\alpha_{\rm MLT}$ was unimportant to their asteroseismic fitting. Since we are interested in young stars, we followed that result, fixing $\alpha_{\rm MLT}$ to 1.9 for all tracks. We adopted the Henyey et al. (1965) formalism for the mixing length, and we did not include element diffusion or thermohaline mixing.

Convective overshoot becomes increasingly important for A-type stars as they approach the terminal-age main-sequence (TAMS). For the models in this work, the important convection zones are a thin one at the surface, and the convective core, each of which should have its own overshooting parameters. Pedersen et al. (2018) discussed appropriate values for the terms f and f_0 for each zone and we adopted the values from Pedersen et al. (2021) in this work. To be specific, we included exponential overshooting at the top of the hydrogen-burning core, with $f = 0.022$ and $f_0 = 0.002$, and we included exponential overshooting in any non-burning shell (i.e. the stellar surface) with $f = 0.006$ and $f_0 = 0.001$. Further description of these terms can be found in the MESA documentation.[1] Since we terminated the evolution one third of the way through the main sequence, the convection parameters are somewhat less important than in many other places on the HR diagram, hence we decided not to vary them. A systematic study of the effect of different convection treatments in δ Sct models will be the subject of future work.

There is some debate on the importance of different stellar atmosphere treatments. Murphy et al. (2021) tried four and found that none affected their asteroseismic age for the pre-MS star HD 139614, at even the 1σ level. Conversely, Steindl et al. (2021) found Eddington–Gray atmospheres were preferred. In this work, we used Eddington T–τ atmospheres. For convergence checking we used the so-called gold tolerances, and we used the dE/dt form of the energy equation.

2.1.3 Sampling the evolutionary tracks

The evolution was broken into different MESA inlists so that sampling parameters could be changed as needed. It is important to keep each time interval in the calculation small so as to minimise computation errors. Until an age of 1 Myr, the evolution was calculated at intervals of 13 kyr, with 15 intervals to each saved sample

[1] https://docs.mesastar.org/en/r15140/index.html

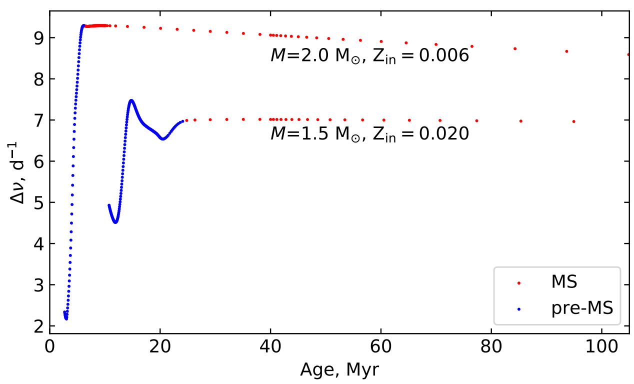

Figure 2. Evolution of $\Delta\nu$ on the pre-MS and early MS, showing the dip that precedes the maximum $\Delta\nu$ value, and the empirical determination of the ZAMS defined in Sec. 2.3. At 40 Myr in both tracks, the switch between age-based sampling and HR-diagram positional sampling can also be seen (Sec. 2.1.3).

for a spacing of 0.2 Myr between samples. In order to sample the rapid changes in evolution (and hence, pulsation frequencies) on the pre-MS, intervals between saved samples were then reduced to every 0.05 Myr until an age of 10.5 Myr. The subsequent evolution is slower and the sampling was decreased to every 3 Myr until 40 Myr. Thereafter, it was limited by changes in position on the HR diagram ($\Delta \log T_{\rm eff} = 0.0006$ and $\Delta \log L = 0.002$), with an upper limit of 100 Myr between samples. Having created these models, the next step was to calculate pulsation frequencies.

2.2 GYRE pulsation calculations

Stellar pulsation frequencies were calculated with GYRE v6.0.1 (Townsend & Teitler 2013; Townsend 2020). We initially calculated these for a representative set of models across the (M, Z) parameter space at all ages. This allowed us to reduce the computational cost of the full grid by ignoring models that did not have $\Delta\nu$ in the region of interest ($\gtrsim 5\,{\rm d}^{-1}$). Specifically, we found that pre-MS stars have a dip in $\Delta\nu$ before reaching their maximum values (Fig. 2), and we calculated pulsation frequencies from ages slightly before this (M-, Z-dependent) age. We used dynamical limits for the frequency range over which modes were calculated, from 1.5× to 12× $\Delta\nu$. Since oscillation frequencies were not available prior to this calculation, $\Delta\nu$ was calculated using the MESA value, which differs a little (Murphy et al. 2021) from the $\Delta\nu$ we ultimately measure with GYRE (Sec. 2.3).

The GYRE calculations use the Magnus Multiple Shooting scheme (Kiehl 1994; Gander & Vandewalle 2007). We performed a linear scan over the described frequency range for up to 100 frequencies – more than sufficient to capture all expected p modes, even if there are many g modes in the same range. After some experimentation to determine optimum scan parameters to preserve accuracy whilst saving computation time, the following scan parameters were used: `x_i` = 0.00001, `w_osc` = 10, `w_exp` = 2, and `w_ctr` = 10.

For each model we calculated adiabatic p-mode frequencies for radial and dipole modes over radial orders $n \sim 1$–11, and a handful of g-mode frequencies. Since the models are non-rotating, we took $m = 0$ for all modes. We also ignored the g modes in the rest of this work.

2.3 Asteroseismic parameters

Reliably inferring the asteroseismic large spacing, $\Delta\nu$, is extremely useful for two reasons: (i) Once $\Delta\nu$ is established, mode identification becomes much easier, because modes of a given degree align vertically in the échelle diagram (Bedding et al. 2020); and (ii) the relation of $\Delta\nu$ to the square root of the mean stellar density tightly constrains age and metallicity.

The other asteroseismic parameter useful in mode identification and model characterisation is ϵ, which parametrizes the positions of different ridges in the échelle diagram. In the asymptotic regime, the stellar oscillation frequencies can be expressed as

$$\nu = \Delta\nu(n + \ell/2 + \epsilon). \qquad (3)$$

While δ Sct stars do not oscillate in the asymptotic regime, they do show equidistantly spaced frequencies (i.e. a large separation) at moderate values of $n \sim 5$–9 (Bedding et al. 2020), and with a $\Delta\nu$ slightly smaller than the truly asymptotic value. We used this to determine $\Delta\nu$ for our model frequencies. Specifically, we fitted a straight line to the radial mode frequencies from $n = 5$ to 9 (inclusive) using linear regression. The resulting gradient is $\Delta\nu$ and the y-intercept is ϵ (White et al. 2011). Bedding et al. (2020) showed ϵ and $\Delta\nu$ to be informative for mass and age estimates on the MS, but pre-MS stars were not discussed. We analyse both evolutionary stages in Sec. 3.

To evaluate trends in pulsation properties occurring at different evolutionary stages, we needed to distinguish pre-MS and MS models. While it is possible to define these stages in terms of core physics (e.g. the point after the CN equilibrium burning bump when nuclear burning accounts for ≥ 1% of the total luminosity; Zwintz et al. 2014), we developed an empirical definition attuned to the pulsation properties by evaluating the evolutionary change in $\Delta\nu$, looking for it to flatten off to its MS value. We first determined the maximum value of $\Delta\nu$ on the MS by applying an age threshold of 30 Myr, and we defined the ZAMS as the first time that the star reaches 95% of this maximum (MS) $\Delta\nu$ and where $0 < d\Delta\nu/dt < 0.5\,{\rm d}^{-1}$/Myr. For stars less massive than 1.65 $M_\odot$ having $Z > Z_\odot$, we also imposed a 20 Myr minimum on the ZAMS age to avoid confusion with pre-MS excursions in $\Delta\nu$, as shown in Fig. 2.

The faster rate at which $\Delta\nu$ changes during the pre-MS necessitated the finer sampling during the early evolution described in Sec. 2.1.3. The grid comprises 573 429 pre-MS and 280 101 MS models. The number of models available in each stage therefore does not correspond to the duration of those stages. Hence, for stellar parameter estimation via asteroseismology (Sec. 4), we used the neural network described in Scutt et al. (2023) that was trained on this grid.

We show the grid on an HR diagram in Fig. 3a. Even without rotation, somewhat different tracks can overlap in the HR diagram (Fig. 3b), explaining why some stars with similar atmospheric parameters can exhibit such different pulsation spectra (Balona 2014).

2.4 Description of the grid data file

We make the grid available as a community resource as a csv file. The grid file contains 853,831 rows, including the column-header row. Descriptions of the columns are provided in the accompanying readme file. All saved MESA profiles are present in the csv file, sorted by evolutionary track – the tracks themselves are sorted by mass, then metallicity. The asteroseismic parameters $\Delta\nu$ and ϵ

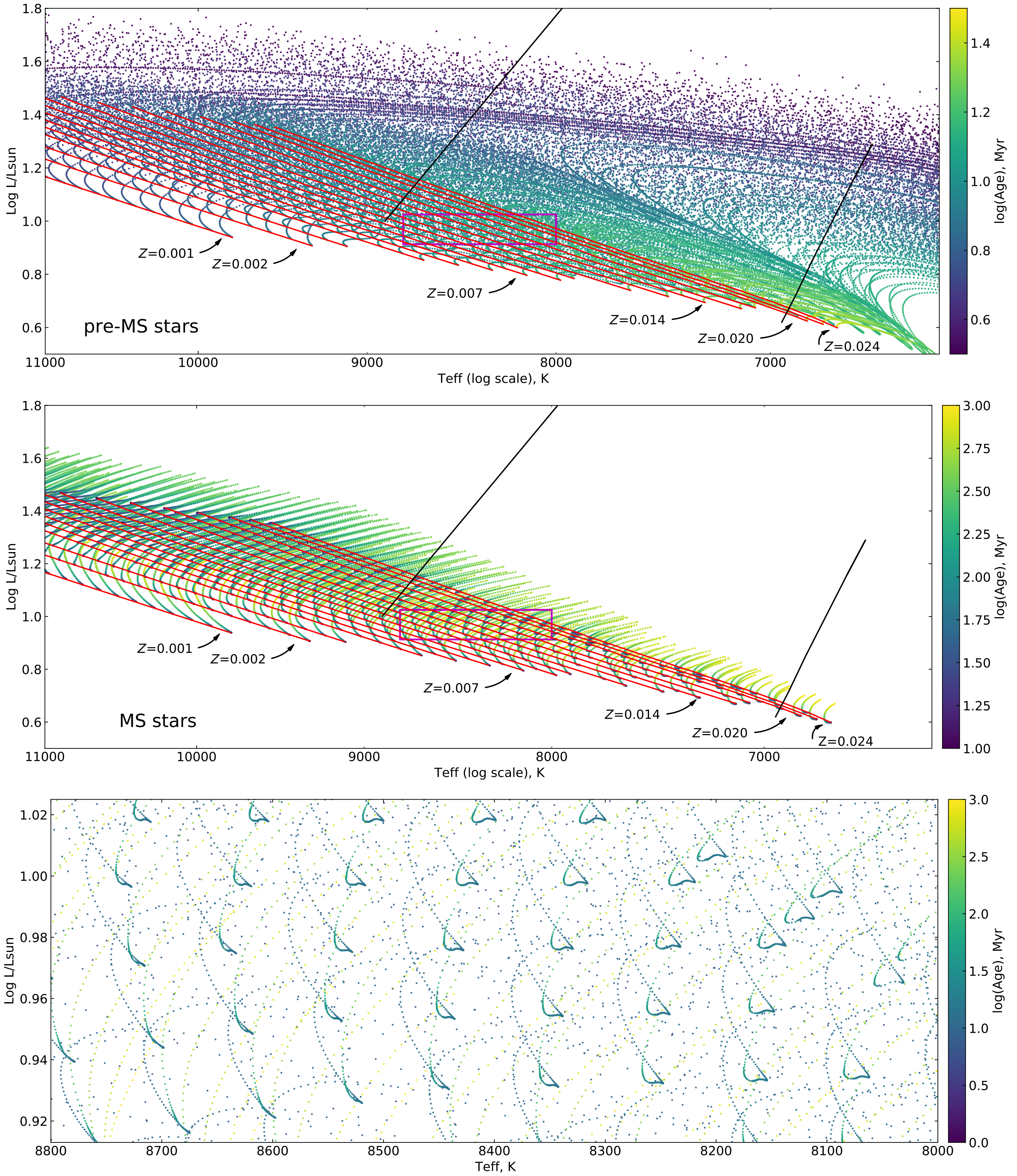

Figure 3. Top: All pre-MS tracks with M>1.45 $M_\odot$, colour-coded by age. The diagonal red lines show the ZAMS labelled by metal mass fraction. The solid black lines are the theoretical instability strip boundaries for solar metallicity from Dupret et al. (2004). The magenta box shows a typical 2σ uncertainty for an observed δ Sct star. Middle: as top, but for MS tracks. Bottom: Zoom at the centre of the instability strip, corresponding to the magenta box in other panels, showing the wide variety of tracks that can represent the typical observed δ Sct star at the 2σ level.

Table 1. Asteroseismic quantities for 15 stars from extended data figure 2 of Bedding et al. (2020). We remeasured the asteroseismic large spacing $\Delta\nu$, the phase parameter ϵ, and the fundamental radial mode frequency f_1 in this work.

TIC	HD	$\Delta\nu$ d^{-1}	ϵ	f_1 d^{-1}	$v \sin i$ $\mathrm{km\,s}^{-1}$
9147509	25369	6.14	1.658	18.96	
11361473	290799	7.72	1.469	22.53	
34737955	44930	6.04	1.655	18.44	
43363194	3622	6.86	1.638	20.39	50 ± 6
44645679	24975	6.21	1.610	18.60	88 ± 4
172193026	46722	6.48	1.684	20.23	
255548143	44958	6.96	1.550	20.57	114 ± 11
259675399	31640	6.63	1.510	19.95	136 ± 4
272951803	187547	6.96	1.648	21.71	10 ± 2
274038922	20203	7.41	1.550	21.74	40 ± 25
287347434	99506	7.06	1.579	21.19	26 ± 2
294157254	55863	6.91	1.568	20.75	99 ± 5
316920092	31901	6.95	1.575	21.07	33 ± 4
388351327	70510	7.24	1.484	21.68	94 ± 10
408906554	42005	7.17	1.564	21.55	130 ± 30

are available for the 800 610 models on which we ran GYRE (see Sec. 2.2).

3 ANALYSIS

3.1 The behaviour of $\Delta\nu$ and ϵ

Even without individual frequency modelling, parametrization of ridges in the échelle diagram can yield useful information about the star. In Fig. 4, we plot the evolution of $\Delta\nu$ and ϵ on the MS as a function of the input parameters, M and Z. To this figure, we add the stars from Bedding et al. (2020, their extended data figure 2), after revisiting all of their échelles to re-determine $\Delta\nu$, ϵ, and f_1 (we provide these in Table 1). We dropped the three stars whose échelles we were unable to model due to insufficiently clear ridges.

We find that Z affects $\Delta\nu$ strongly but has little effect on ϵ: the arrow marking the Z dependence in Fig. 4 lies almost parallel to the $\Delta\nu$ axis. Conversely, mass has little effect on $\Delta\nu$ but somewhat more on ϵ. We discuss this further in Sec. 3.3. Thus, mass and metallicity are somewhat orthogonal in this plane, which is why $\Delta\nu$ and ϵ are useful asteroseismic parameters. There is also an age dependence whose vector lies at an angle to that of the other parameters. The simplicity of Fig. 4 suggests that machine learning based solely on these asteroseismic observables should perform quite well for MS stars (S. Kumar Panda, in prep.). The inclusion of a temperature variable would also offer greater sensitivity to mass.

The same diagram is somewhat more complicated for pre-MS stars, where the dependence on age is no longer monotonic for either parameter (Fig. 5). At the youngest ages of a given evolutionary track (M–Z pair), $\Delta\nu$ changes little with evolution while ϵ grows rapidly from the minimum to the maximum value of its observed range. A turning point is soon encountered, though, after which age and Z share importance in determining $\Delta\nu$. To further complicate matters, low-mass and high-metallicity tracks behave differently from most others in the grid, undergoing an excursion to very low values of ϵ.

Although the range in ϵ is greater for the pre-MS models, this is really just for the initial contraction, where $\Delta\nu$ is small. The majority of the pre-MS stage is contained within a dense region of points having $\Delta\nu \sim 5$–10 and $\epsilon \sim 1.4$–1.7. A comparison of Figs 4

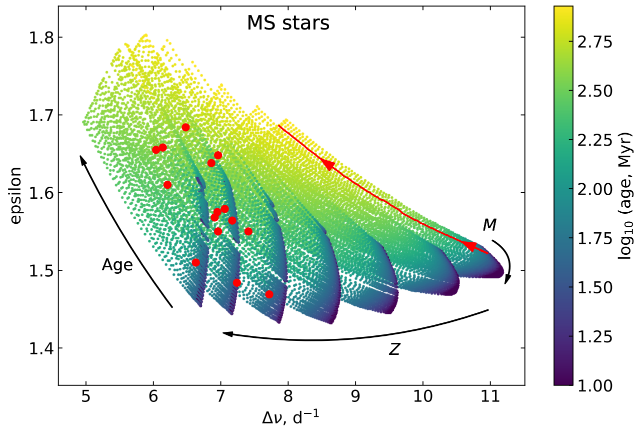

Figure 4. Evolution of $\Delta\nu$ and ϵ on the main sequence, showing dependence on mass, metallicity, and age in a predictable, monotonic way. Models shown here have $M \geq 1.53\,\mathrm{M}_\odot$ and $Z \geq 0.002$. Tracks have been thinned in metallicity for clarity. The evolutionary track at $M = 1.60\,\mathrm{M}_\odot$ and $Z = 0.002$ is shown as a red line. The 15 stars from Table 1 are shown as red circles.

& 5 shows that this is the same region occupied by the MS models. This is somewhat expected, given that the MS evolutionary tracks evolve back in the direction from whence they came on the pre-MS (Fig. 3), but it makes distinguishing MS and pre-MS stars difficult when only $\Delta\nu$ and ϵ are used. The full set of pulsation frequencies, however, is able to distinguish these two stages in the vast majority of cases, and a neural network is still able to learn to emulate the models either side of the ZAMS (Scutt et al. 2023).

3.2 Scaling Relations

For solar-like oscillations, which are excited stochastically by convection, there are two widely-used scaling relations (see review by Hekker 2020). The first concerns $\nu_{\rm max}$, the frequency of maximum oscillation power, which is observed to scale as $g/\sqrt{T_{\rm eff}}$.

The modes of δ Sct stars are not stochastically driven and our understanding of driving and damping is poorly understood. Evidence of the latter comes from published mode identifications where ridges are identifiable but incomplete: Murphy et al. (2021) showed that only half of the radial modes are detected in HD 139614, and we provide a similar example in Sec. 4 using HD 31901 which is missing half its dipole modes. Hence, we did not design our grid with the intention of modelling the overall excitation behind δ Sct p modes (for such an analysis, see Steindl et al. 2021), and so we do not have the necessary information to model the frequency of maximum power, $\nu_{\rm max}$. Some studies have suggested that a $\nu_{\rm max}$–$T_{\rm eff}$ relation exists for δ Sct stars (Barceló Forteza et al. 2018, 2020; Hasanzadeh et al. 2021), but TESS observations of 36 Pleiades δ Sct stars (of the same age and metallicity) seem to rule out a simple relation (Bedding et al. 2023). Instead, we turn our attention to further characterising the second scaling relation, which relates $\Delta\nu$ to the square root of the mean stellar density.

In Fig. 6 we plot departure of $\Delta\nu$ from the scaling relation, following eq. 5 of Sharma et al. (2016):

$$f_{\Delta\nu} = \left(\frac{\Delta\nu}{\Delta\nu_\odot}\right)\left(\frac{\rho}{\rho_\odot}\right)^{-0.5}. \qquad (4)$$

Unlike solar-like oscillators, which have $f_{\Delta\nu}$ within a few percent of

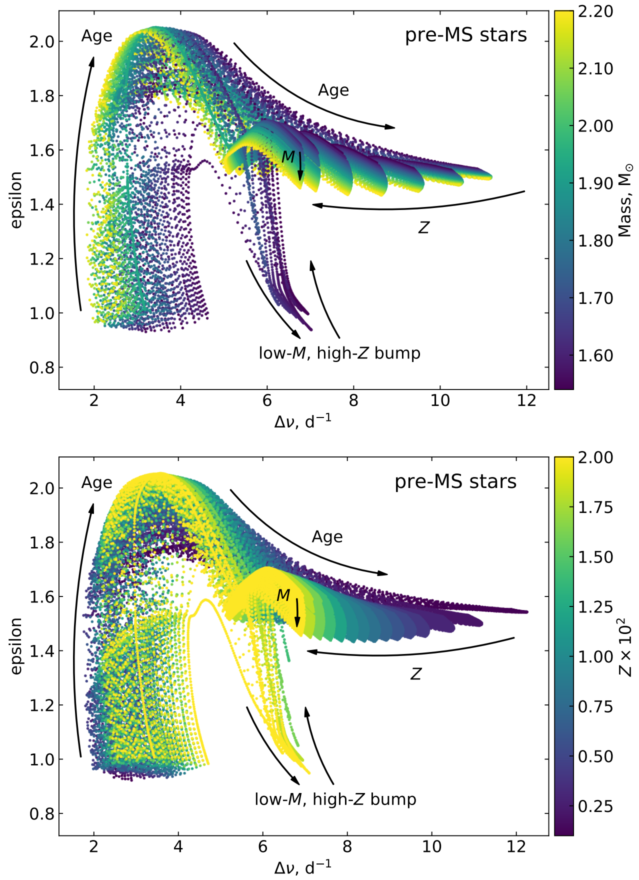

Figure 5. The evolution of $\Delta\nu$ and ϵ on the pre-MS, showing dependence on mass, metallicity, and age. Models in the top panel are thinned like in Fig. 4 and colour-coded by mass, whereas in the bottom panel all values of $Z \leq 0.02$ are shown and colour coding is by metallicity. This upper limit allows the low-M high-Z bump to be seen clearly (see Sec. 3.1). Arrows on this bump show the direction of increasing age.

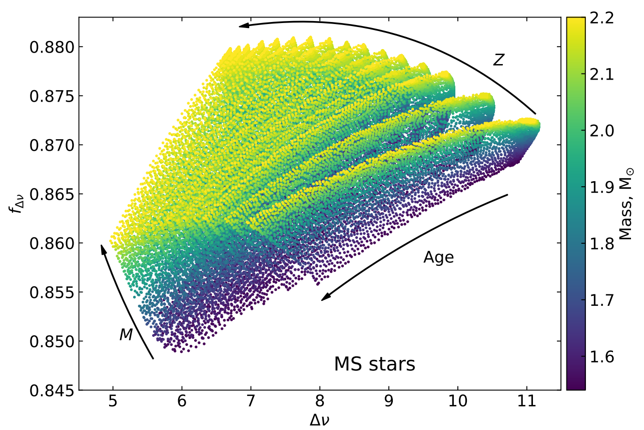

Figure 6. Departure of $\Delta\nu$ from the asteroseismic scaling relation. There is a systematic offset of ∼0.865 with small but predictable perturbations according to mass, metallicity, and age. Models shown here have $M \geq 1.53\,\mathrm{M}_\odot$ and $Z \geq 0.002$.

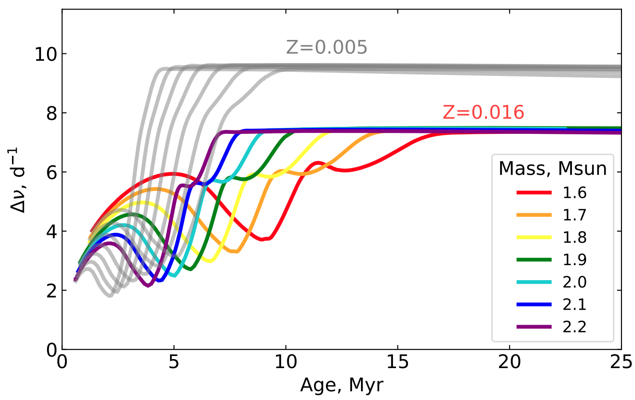

Figure 7. The evolution of $\Delta\nu$ as a function of age. Coloured lines represent different masses at Z=0.016; grey lines show the same set of masses at a different metallicity (Z=0.005). The MS value of $\Delta\nu$ is dependent only on metallicity; mass has very little effect. This can also be seen by the orthogonality of the mass and metallicity data axes in Figs 4 & 5.

unity (White et al. 2011; Hekker 2020; see also Guggenberger et al. 2016; Rodrigues et al. 2017; Serenelli et al. 2017; Pinsonneault et al. 2018), we determine that the δ Sct stars have $f_{\Delta\nu} \sim 0.87$. Suárez et al. (2014) previously determined in a general sense that for δ Sct stars $\Delta\nu/\Delta\nu_\odot = 0.776(\rho/\rho_\odot)^{0.46}$. Here, we show that there is clear dependence of $f_{\Delta\nu}$ on our three independent variables, M, Z, and age. Hence, not only do our models support the existence of a $\Delta\nu$ scaling relation, but they indicate that departures from it might carry information on specific parameters. Ultimately, now that mode identification has become tractable and modelling has become quick (Scutt et al. 2023), δ Sct modelling might skip the era of scaling relations and proceed directly to frequency modelling.

3.3 The ZAMS $\Delta\nu$ is insensitive to Mass

Our models show that the MS value of $\Delta\nu$ is dependent only on metallicity – mass has very little effect. Fig. 7 shows this mass independence, and also shows that once stars reach the ZAMS, their densities plateau. They do this for around 100 Myr before they more quickly decrease with age. Because these stars are close to the ZAMS, their isochrones lie parallel to the ZAMS, hence any mass difference has had little differential effect on the stellar evolution. It is interesting that stars of such a wide range of masses arrive on the ZAMS with almost identical densities. Fig. 8 shows that isochrones lie parallel to isodensity contours, to a good approximation.

We explored this numerically in more detail. Within the instability strip (at $T_{\rm eff}$ between 7000 and 9000 K), the density of a 100-Myr isochrone never deviates from its average value of $0.547\rho_\odot$ by more than 1.25%. Since $\Delta\nu \propto \sqrt{\rho}$, then $\Delta\nu$ should be constant to around 0.6% (or $0.04\,\mathrm{d}^{-1}$) for a given metallicity. It is remarkable that this occurs despite spanning a mass range of 20%. In young clusters such as the Pleiades, this means that rotation is the only factor causing differences in $\Delta\nu$. At rotation velocities of $150\,\mathrm{km\,s}^{-1}$, the difference in density between a static and a rotating model reaches around 8% (Murphy et al. 2022), so $\Delta\nu$ should differ by approx $0.3\,\mathrm{d}^{-1}$ for rapid rotators. The observed spread in $\Delta\nu$ values currently sits at $0.15\,\mathrm{d}^{-1}$ for Pleiades stars with $\Delta\nu$ measurements (Murphy et al. 2022).

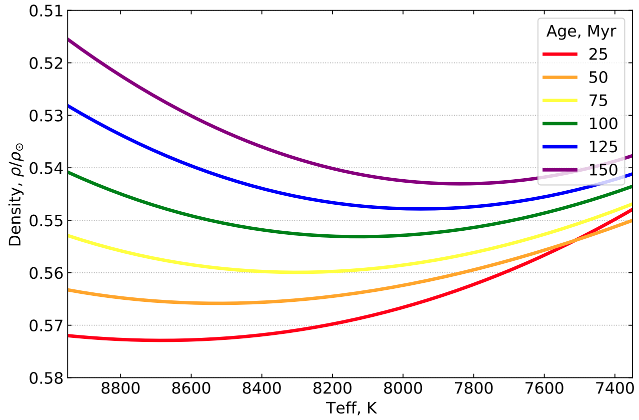

Figure 8. Isochrones for the early MS at 25 Myr spacing, made from tracks of solar metallicity ($Z = 0.014$) at masses of 1.38 to 1.70 $M_\odot$. The isochrones are almost flat, having turning points in density over a wide range of temperatures covering the δ Sct instability strip. Consecutive isochrones have very similar shapes, despite spanning a wide mass range. Hence, an isochrone for a given metallicity has a nearly constant density as a function of mass and temperature across the instability strip.

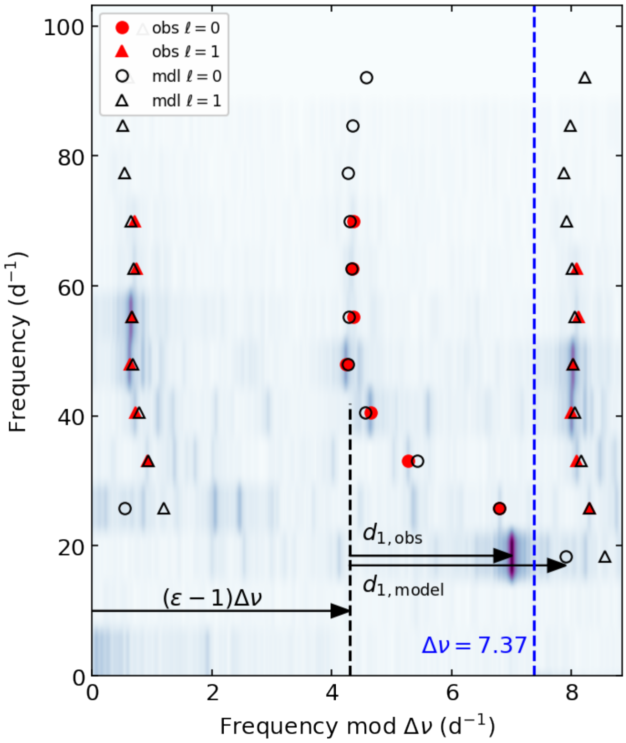

Figure 9. An illustration of the mismatch between models and observations for the fundamental radial mode. using HD 20203. We also introduce the d_1 parameter, which describes the curvature of the radial ridge at low radial orders. We show d_1 for the strong peak at low frequency and for the best-fitting model from the grid. Neither the radial nor the dipole mode at $n = 1$ are well modelled.

3.4 The fundamental radial mode is poorly modelled

In many multi-periodic stars, the observed frequency of the fundamental radial mode (f_1) is poorly modelled, including the well-studied pre-MS star HD 139614 (Murphy et al. 2021; Steindl et al. 2022, see also Sec. 4.1, this work), the otherwise well-modelled star HD 99506 (Scutt et al. 2023), and two of the five stars modelled in Sec. 4. This is alarming because one of the traditional ways of identifiying modes is to compare the period ratios of low-frequency p modes against those computed with models of radial modes, especially via so-called Petersen diagrams (Petersen & Christensen-Dalsgaard 1996; Suárez et al. 2006; Netzel et al. 2022). The stars mentioned above have models that match well for the entire radial ridge but not for f_1.

Here, we attempt to characterise differences between obvious candidates for f_1 (strong peaks at roughly the expected frequency) and their equivalent model frequencies. We use HD 20203 to illustrate a particularly egregious mismatch. This star has 14 modes that match models very well, but the strong peak near f_1 is a poor fit (Fig. 9). Although we focus our efforts on the radial mode for simplicity, we have also noticed that matches for the lowest-order dipole mode are often poor, such as in HD 20203. Perhaps it is the absence of rotation in our models that causes the lowest order (deepest penetrating) modes to fit poorly, since they have the longest wavelengths and might therefore exhibit the greatest sensitivity to any global asphericity.

Other methods for identifying f_1 also exist. In Bedding et al. (2020, their extended data figure 2), f_1 was observed to lie at a frequency of approximately $3\Delta\nu$. Our model grid shows this to be a good approximation (Fig. 10). Generally, f_1 exceeds $3\Delta\nu$ by a few percent, hence one should expect the radial mode to lie on the LHS of row four of the échelle (or 0–1 d^{-1} to the right of the dashed line of row three in our phase-wrapped échelles). It is rare for f_1 to lie at frequencies lower than $3\Delta\nu$ in our models, especially at higher metallicity. Murphy et al. (2020) used the $3\Delta\nu$ approximation and the rest of the radial ridge in échelle diagrams to identify the radial mode in 11 pulsating TESS λ Boo stars and used either Petersen diagrams or the Period–Luminosity relation (McNamara 1997; Ziaali et al. 2019; Barac et al. 2022) to identify the fundamental mode in 17 others. It is noteworthy that while Murphy et al. (2020) sometimes identified the fundamental mode using two techniques for the same star, Petersen diagrams (i.e. period ratios) and échelle diagrams were not successfully applied together.

To further investigate the aforementioned common mismatch, we define a new quantity, d_1, describing the departure of the fundamental radial mode, f_1, from the radial ridge in an échelle diagram. As shown in Fig. 9, it measures the curvature of the radial ridge at low radial orders. The x-location of the radial mode ridge is already established via the asteroseismic parameters ϵ and $\Delta\nu$ (see Sec. 2.3), hence

$$d_1 = f_1 - (\epsilon + 1)\Delta\nu. \quad (5)$$

By defining d_1 in this way, it is insensitive to the natural variation of ϵ between stars, unlike the quantity $f_1/3\Delta\nu$, which is simultaneously ϵ and $\Delta\nu$ dependent. In Fig. 11 we plot d_1 in the dimensionless form $d_1/\Delta\nu$ for models in our grid, separated into pre-MS and MS stages of evolution. To this figure, we have again added the 15 stars from Table 1, and we note that their evolutionary states (pre-MS vs. MS) are unknown.

As expected, HD 20203 is one of the outliers in Fig. 11, indicating that the strong peak at 21.75 d^{-1} is incompatible with the fundamental radial mode in our models. We do not expect this to be fixed by the inclusion of rotation, since a change large enough to shift f_1 by $\sim$1 d^{-1} will also change other mode frequencies substantially.

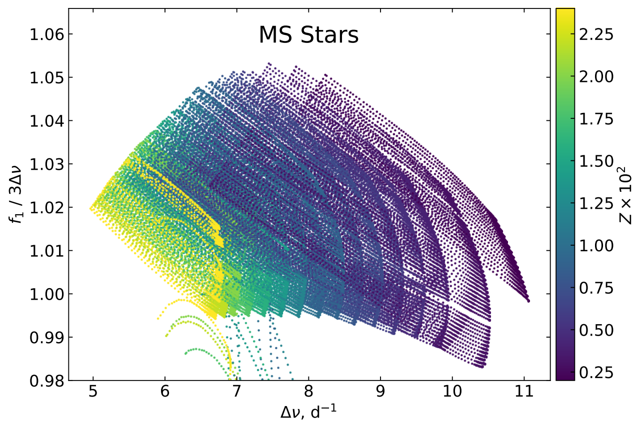

Figure 10. The ratio of the fundamental radial mode frequency, f_1, to three times the large frequency separation, $3\Delta\nu$, for MS models in the grid. The smattering of points at $\Delta\nu \sim 7$ with $f_1/\Delta\nu < 0.995$ are mislabelled pre-MS models.

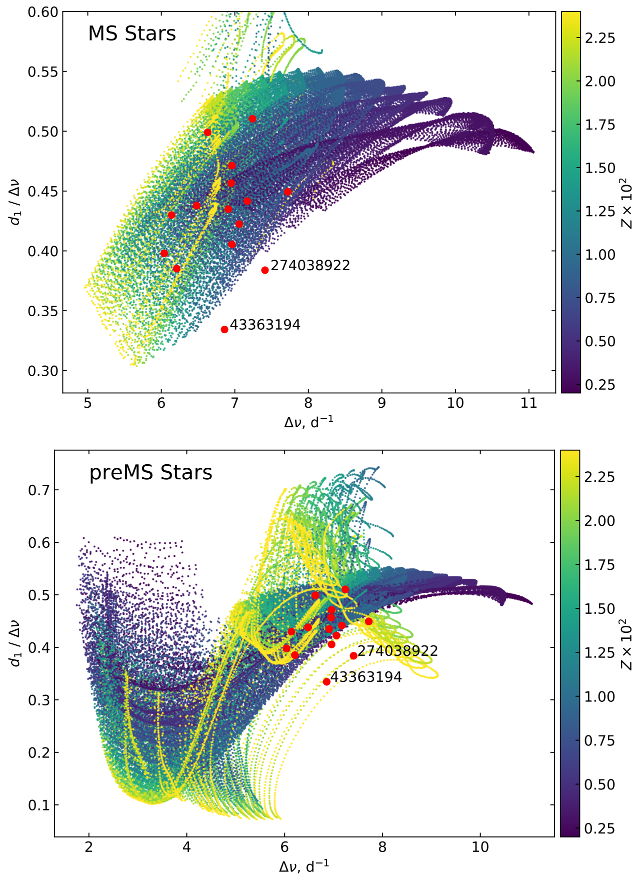

Figure 11. The d_1 parameter for MS and pre-MS stars. Note that the panels have different axis ranges but a common colour bar. Red circles show the 15 stars from Table 1. Outliers are TIC 274038922 = HD 20203, and TIC 43363194 = HD 3622.

In summary, the d_1 parameter is a useful check on whether the f_1 has been correctly identified. Agreement with models is a necessary (but insufficient) condition for correct identification of f_1. The d_1 parameter may also help to diagnose any mismatch of f_1.

4 APPLICATION TO REAL STARS

Preliminary versions of the grid have already been used to model several stars, including the superjovian-exoplanet host HIP 99770 (Currie et al. 2023), three stars in the new Cepheus Far North association (TIC 373018187, TIC376872090, and TIC 429019921; Kerr et al. 2022a), five members of the Pleiades star cluster (Murphy et al. 2022), and HD 21434 in the Fornax–Horologium association (Kerr et al. 2022b). Here we apply the grid to six additional stars to demonstrate its utility. We use the neural network described in Scutt et al. (2023) to perform the Bayesian inference and to provide quantitative uncertainties on mass, age, and metallicity.

For all stars modelled here, the likelihood of the observations, given the input model parameters, θ, is given by eq. 4 of Scutt et al. (2023)

$$\log \mathcal{L}(D|\theta) = \log \mathcal{L}(D_{\rm S}|\theta) + \log \mathcal{L}(D_{\rm C}|\theta), \quad (6)$$

which we separate into the seismic contribution, $D_{\rm S}$, and classical (non-seismic) contributions $D_{\rm C}$, comprising of the effective temperature $T_{\rm eff}$ and luminosity L. The contribution to the likelihood of the mode frequencies is given by

$$\log \mathcal{L}(D_{\rm S}|\theta) = \sum_i \log \mathcal{N}\left(\nu_i^{\rm obs}, \sqrt{\sigma^2_{\nu_i^{\rm obs}} + \sigma^2_{\nu_i^{\rm NN}}}\right), \quad (7)$$

and that of the classical observables is given by

$$\log \mathcal{L}(D_{\rm C}|\theta) = \log \mathcal{N}\left(\log L^{\rm obs}, \sqrt{\sigma^2_{L^{\rm obs}} + \sigma^2_{L^{\rm NN}}}\right) + \log \mathcal{N}\left(T_{\rm eff}^{\rm obs}, \sqrt{\sigma^2_{T_{\rm eff}^{\rm obs}} + \sigma^2_{T_{\rm eff}^{\rm NN}}}\right) \quad (8)$$

(Scutt et al. eqs 5 & 6). The intrinsic uncertainty arising from the neural network representation of the data, $\sigma_{\rm NN}$, is captured in each case. Further details can be found in Scutt et al. (2023).

4.1 A worked example: HD 139614

We start with the protoplanetary disk host HD 139614, which has been modelled by both Murphy et al. (2021) and Steindl et al. (2022). The mode IDs were common across both studies, though Steindl et al. also labelled the mode at 20.599 d^{-1} as the fundamental radial mode, where Murphy et al. had declined to use it because it didn't match their models. We note here that $d_1/\Delta\nu = 0.442$ for that mode, which is compatible with both the pre-MS and MS distribution in Fig. 11, but nonetheless we find it incompatible with the other (well-matched) ids. Another main difference between these two studies was the helium abundance. Murphy et al. fixed the helium abundance to $Y = 0.29$, whereas Steindl et al. allowed a very broad range from 0.216 to 0.282, half of which lies below the primordial helium abundance from big bang nucleosynthesis. In this work, helium abundance is a function of metal abundance (Sec. 2.1.1), which for a star of $Z = 0.0100$ results in $Y = 0.2741$. Finally, Steindl et al. used three modelling approaches with regards to the classical observables: one where only a 1σ box was taken around the observed values (i.e. the approach used by Murphy et al. 2021);

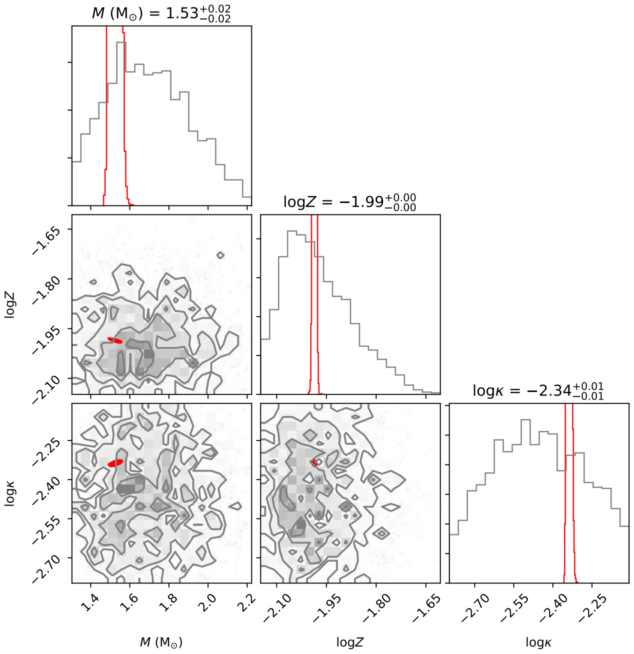

Figure 12. The sampled priors applied when modelling HD 139614 (grey contours and histograms). Also shown are the posterior distributions for HD 139614 (red), which are contained well within the bounds of those priors. The parameters are described in Sec. 4.1.

another where a 3σ box was used; and a final approach where the χ^2 of the classical observables was added to the asteroseismic χ^2 (their eq. 7). We agree with Steindl et al. that the 1σ approach is too narrow. Our approach here is similar to their χ^2 addition formula, except that we do not need to specify χ^2 thresholds based on p values.

Compared to other stars we model here, we treated HD 139614 as a special case because it has a measured metallicity in the literature and it has already been modelled asteroseismically. As Murphy et al. (2021) mentioned, the literature [Fe/H] value (-0.57 ± 0.13, Folsom et al. 2012) is somewhat biased by a chemical peculiarity of the λ Boo type (Kama et al. 2015), and does not correspond to the best-fitting asteroseismic solution. Nonetheless, we did not wish to exclude asteroseismic solutions that would match the lower spectroscopic [Fe/H] value. We therefore chose for our beta-distribution prior on $\log Z$: $\beta_6^2(-2.15, 0.7)$. We plot all of our priors in Fig. 12. For the age prior, rather than following Murphy et al. (2021) and imposing a flat prior with a maximum age of 30 Myr, we chose a prior that strongly preferences ages compatible with its membership in Upper Centaurus–Lupus. UCL has a median cluster age of 16 ± 2 Myr (Pecaut & Mamajek 2016), with a 1σ age spread of 7 Myr (Mamajek et al. 2002; Preibisch & Mamajek 2008; Pecaut & Mamajek 2016), and HD 139614 has an asteroseismically measured age of 10–12 Myr (Murphy et al. 2021; Steindl et al. 2022). Specifically, we adopted $\log \mathcal{K}$: $\beta^2_{1.2}(-3, -0.3)$ for this star (see Scutt et al. 2023 for details). For the mass prior we used the beta distribution in Scutt et al., namely $M[\mathrm{M}_\odot]$: $\beta_3^2(1.3, 2.3)$, which allows any mass between $\sim$1.3 and 2.2 $\mathrm{M}_\odot$. The best-fitting solution is contained well within these priors (Fig. 12).

We found a best-fitting mass of $1.53 \pm 0.02\,\mathrm{M}_\odot$, a metal mass fraction of $Z = 0.0103 \pm 0.0001$ and an age of 11.87 ± 0.33 Myr. We emphasize that the uncertainties only represent the random uncertainty, including that inherent within the neural network itself. Systematic uncertainty pertaining to model physics remains unaccounted for because it is not well understood, and a thorough analysis of that uncertainty is urgently needed. Nonetheless, we can see that the resulting age is intermediate between that of Murphy et al. (2021) and Steindl et al. (2022) (10.75 ± 0.77 and 12 ± 3 Myr, respectively), probably as a result of having an intermediate helium abundance. The application of the neural network has halved the random uncertainties.

4.2 Further examples

We also re-examined three stars from Bedding et al. (2020) with measured $v \sin i$: the slow rotator HD 31901 ($33 \pm 4\,\mathrm{km\,s^{-1}}$), the moderate rotator HD 55863 ($v \sin i = 99 \pm 5\,\mathrm{km\,s^{-1}}$), and the rapid rotator HD 28548 ($v \sin i = 200 \pm 50\,\mathrm{km\,s^{-1}}$). The latter demonstrates that the non-rotating grid can still aid mode IDs for rapid rotators. We also examined two stars whose rotation rates have not been measured: HD 46722, also from the Bedding et al. (2020) sample, which has an exceptionally long radial ridge in its échelle (n = 1–9), and HD 112063, with 8 dipole modes and 8 radial modes (this work). The Fourier transforms of TESS lightcurves of these five stars are shown in Fig. 13 with their modes labelled. Those labelled mode frequencies are given in Table 2.

We analysed all of these stars with the default priors on mass, age, and metallicity from Scutt et al. (2023). We used Gaussian priors on temperature and luminosity, specified in Table 3, and we report the posterior probability estimates for their stellar parameters in Table 3. Plots of these estimates are shown in the Appendix (Figs A1–A3). We found that three stars (HD 31901, HD 55863, HD 28548) have young MS ages, whereas HD 46722 and HD 112063 are in their pre-MS stage.

4.2.1 HD 31901

HD 31901 was modelled superficially by Bedding et al. (2020), who noted it as a member of the recently discovered Pisces–Eridanus stream Meingast et al. (2019). This association has been measured to be about 120 Myr old by gyrochronology (Curtis et al. 2019) and this age has been supported by asteroseismology of HD 31901 (Bedding et al. 2020). In a thorough spectroscopic analysis, Hawkins et al. (2020) measured a metallicity of [Fe/H]$= -0.03 \pm 0.07$, which also supported an age of $\sim$120 Myr, while the best-fitting kinematic age is slightly older at $\sim$135 Myr (Röser & Schilbach 2020).

Of the five stars we study in detail here, HD 31901 has the fewest identified modes, though it has much untapped potential via a prograde $\ell = 1$ ridge. Naturally, we are unable to model prograde modes using non-rotating models. When analysed using the standard priors, the best-fitting metallicity was $Z = 0.0211$, somewhat larger than expected from the literature values above. We re-ran our analysis, attempting to model the star with a tight solar metallicity prior $Z \approx 0.0144$, but we were unable to obtain a good fit. We note that the posteriors indicated an inverse correlation between metallicity and age, which suggests an age of around 120 Myr at $Z \sim 0.019$. Hence, asteroseismology strongly supports a young MS age, rather than the 1-Gyr age suggested for the Pisces–Eridanus stream by Meingast et al. (2019).

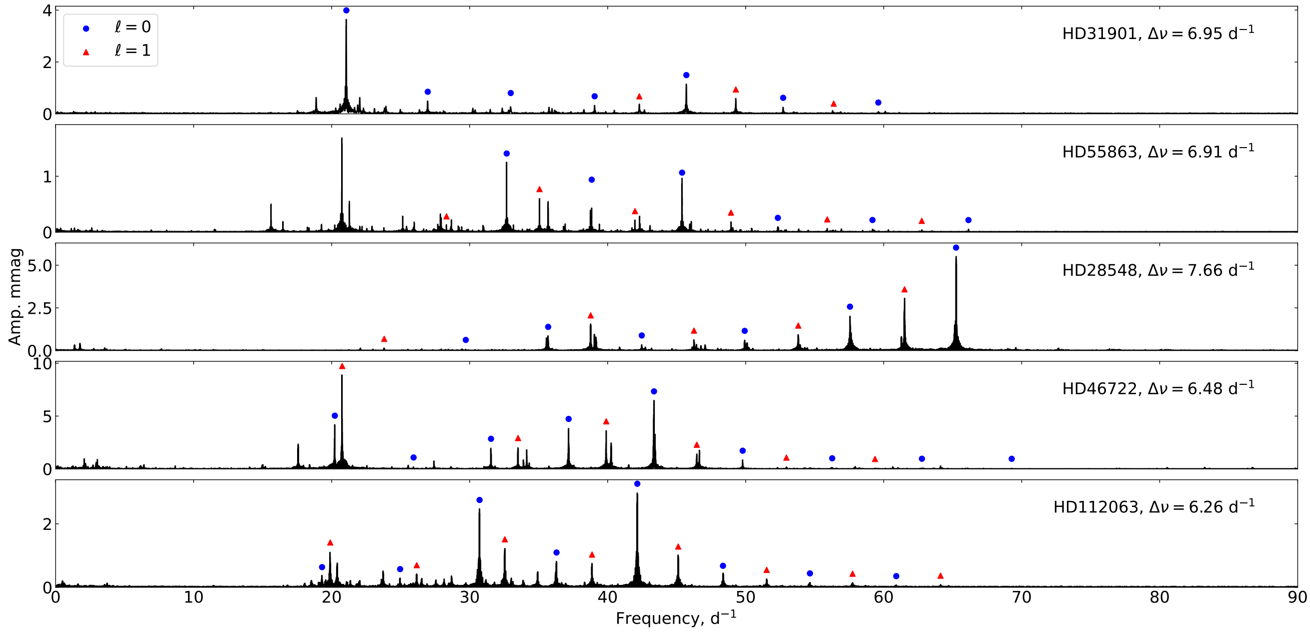

Figure 13. Fourier transforms of the TESS light curves of five of the δ Sct stars modelled in this work (Sec. 4.2). Blue circles and red triangles label their radial and dipole modes, respectively. These mode IDs are given in Table 2.

Table 2. Mode IDs for the five stars analysed here for the first time (Sec. 4.2).

HD 31901				HD 55863				HD 28548				HD 46722				HD 112063			
Freq. d^{-1}	Amp. μmag	n	ℓ	Freq. d^{-1}	Amp. μmag	n	ℓ	Freq. d^{-1}	Amp. μmag	n	ℓ	Freq. d^{-1}	Amp. μmag	n	ℓ	Freq. d^{-1}	Amp. μmag	n	ℓ
21.0658	3628	1	0	32.6853	1240	3	0	29.7205	76	2	0	20.2317	4152	1	0	19.3056	342	1	0
26.9651	489	2	0	38.8456	772	4	0	35.6892	839	3	0	25.9366	200	2	0	24.9626	280	2	0
32.9783	440	3	0	45.3935	898	5	0	42.4728	337	4	0	31.5481	1965	3	0	30.7183	2457	3	0
39.0582	316	4	0	52.3324	89	6	0	49.9313	607	5	0	37.1734	3845	4	0	36.2954	803	4	0
45.7033	1133	5	0	59.1888	51	7	0	57.5579	2023	6	0	43.3591	6451	5	0	42.1488	2968	5	0
52.7157	256	6	0	66.1454	50	8	0	65.2462	5483	7	0	49.7844	840	6	0	48.3568	383	6	0
59.6106	74	7	0	28.3225	116	2	1	23.8091	140	1	1	56.2692	124	7	0	54.6575	145	7	0
42.2948	315	4	1	35.0640	603	3	1	38.7703	1515	3	1	62.7715	81	8	0	60.9121	58	8	0
49.2877	579	5	1	41.9811	210	4	1	46.2566	623	4	1	69.2775	75	9	0	19.8986	1118	1	1
56.3789	33	6	1	48.9356	183	5	1	53.8129	917	5	1	20.7644	8850	1	1	26.1657	403	2	1
				55.9122	62	6	1	61.5114	3040	6	1	33.5084	2036	3	1	32.5512	1218	3	1
				62.7613	36	7	1					39.8974	3620	4	1	38.8685	737	4	1
												46.4600	1410	5	1	45.1138	989	5	1
												52.9526	189	6	1	51.5212	255	6	1
												59.3739	60	7	1	57.7478	135	7	1
																64.1219	72	8	1

Table 3. Priors and outputs on stellar parameters.

Star	Input		T_{eff} & L source	Output		
	T_{eff} ± err K	L ± err $L_{\odot}$		M ± err $M_{\odot}$	Z ± err	Age ± err Myr
HD 31901	7770 ± 250	7.74 ± 0.39	Bedding et al. (2020)	1.71 ± 0.02	0.0211 ± 0.0001	$45.04^{+9.48}_{-9.01}$
HD 55863	7650 ± 250	7.80 ± 0.38	Bedding et al. (2020)	1.75 ± 0.02	0.0217 ± 0.0002	$37.73^{+12.51}_{-8.59}$
HD 28548	8510 ± 250	10.82 ± 0.55	Bedding et al. (2020)	1.84 ± 0.02	0.0144 ± 0.0001	$15.10^{+2.67}_{-2.67}$
HD 46722	7810 ± 250	8.28 ± 0.40	Bedding et al. (2020)	1.51 ± 0.01	0.0076 ± 0.0003	$9.04^{+0.23}_{-0.25}$
HD 112063	7517 ± 250	6.98 ± 0.30	Stassun et al. (2019)	1.61 ± 0.01	0.0189 ± 0.0002	$16.00^{+0.33}_{-0.30}$

4.2.2 HD 55863

This star was one of the examples with mode IDs in Bedding et al. (2020, see their extended data figure 1), and also appears to have a prograde dipole ridge. We modelled twelve modes, consisting of six consecutive radial orders of the radial and dipole ridges. HD 55683 has a moderate $v \sin i$ and might make a simple case for study with models that include rotation.

4.2.3 HD 28548

This is a λ Boo star with a large infrared excesses in the WISE W3 (19σ) and W4 (15σ) bands (Gray et al. 2017). Bedding et al. (2020) matched this star to a model of mass $1.59\,M_\odot$ and age 270 Myr. Our model is more massive and younger (see Table 3). The temperature determined from Strömgren photometry by Murphy et al. (2020, 8490 ± 170 K) is very similar to the one we used here, but their luminosity at $10.04\,L_\odot$ is somewhat smaller than the one we used from Bedding et al. (2020). We report values based on the Bedding et al. (2020) inputs. We repeated our analysis of this star using the parameters from Murphy et al. (2020) and found that the resulting metallicity and age were the same within 1σ, but the lower luminosity resulted in a lower mass by 2σ. The bulk (asteroseismic) metallicity we measure for HD 28548 is solar, which suggests that the spectroscopic metal-line weakness, also reflected in the Strömgren photometry, is only skin-deep. This marks the second demonstration (following HD 139614; Murphy et al. 2021) that the λ Boo phenomenon is confined to the stellar surface, as suspected from ensemble studies (Paunzen et al. 2015; Murphy et al. 2020).

4.2.4 HD 46722

This is a λ Boo star with an observed infrared excess (Gray et al. 2017). Murphy et al. (2020) calculated stellar properties from isochrones, using a luminosity derived from Gaia parallaxes and temperatures derived from Strömgren photometry. This implied a solar metallicity, [Fe/H]$= -0.016^{+0.12}_{-0.14}$. The metallicity we derive here ($Z = 0.0076 \pm 0.0003$) is the lowest in our sample and corresponds to [Fe/H]$= -0.26$, using Asplund et al. (2009) solar abundances. The fact that the bulk metallicity is lower than the surface metallicity is inconsistent with the λ Boo classification, perhaps representing a limitation in the Strömgren method for a dusty star, or reflecting the unmodelled stellar rotation. A further possibility is that the observed luminosity has been strongly affected by extinction, and this in turn is influencing our Bayesian inference on the asteroseismology. We note that this star's Gaia RUWE value is small (0.96) suggesting it is not a binary, hence the luminosity is much more likely to be underestimated (due to dust) than overestimated (due to a companion).

4.2.5 HD 112063

This is also a λ Boo star, although without an infrared excess (Gray et al. 2017). Contrary to its metal-weak spectrum, we find that the bulk metallicity is slightly above solar. Its long ridges without any missing modes represent the mode complete mode ID for a δ Sct star to date (Fig. A4).

4.3 Posterior frequency predictions

We show posterior predictions for each mode frequency on the échelle diagrams in Fig. A4 as grey symbols. the spread in posterior frequencies gives a good indication of how well the model is constrained. The red symbols on the échelles show the observed frequencies that were used as constraints for the neural network, which we expect to lie within the range of predicted frequencies. If not, it suggests that a mode has been misidentified. The $n = 2$ radial mode for HD 31901 would seem to be such a misidentified mode, perhaps because the star does not pulsate in this mode, or perhaps the identification is correct but the mismatch arises from neglecting rotation. These diagrams can also highlight any weaker peaks that lie within the distribution of posterior predicted frequencies, and which might be used in a second iteration of mode identification. An example of such a mode could be the $n = 1$ dipole mode in HD 31901. However, in this work we only performed one iteration, using the most obvious mode identifications, lest we 'reinforce' any emerging best-fitting model from early iterations.

5 CONCLUSIONS

We have presented and made available a grid of stellar models for δ Scuti stars, with mass, metal mass fraction and age as the independent variables. We computed the asteroseismic parameters $\Delta\nu$ and ϵ for 800 000 models and examined how they depend on the independent variables (Figs 4 & 5). The orthogonality of the mass and metallicity vectors in the $\Delta\nu$–ϵ plane makes these parameters useful when individual frequency modelling is not possible. Specifically, at the ZAMS, ϵ is determined almost exclusively by mass and $\Delta\nu$ is determined almost exclusively by metallicity. In other words, models of a given metallicity have the same $\Delta\nu$ at the ZAMS regardless of their mass. Some regularities in $\Delta\nu$ and ϵ are also seen in the pre-MS stage but there are more caveats to beware of. We also determined that $\Delta\nu$ for MS δ Sct stars deviates from the $\Delta\nu$ scaling relation by 13% (Fig. 6).

We described a tendency for the fundamental radial mode, and sometimes the $n = 1$ dipole mode, to be poorly fitted by our models. The radial ridge in an échelle diagram can be modelled well in many cases, but the fundamental radial mode is rarely matched. We have introduced a parameter, d_1, which measures the curvature at the bottom of the radial ridge, to help diagnose this and to aid mode identification. We computed the distribution of d_1 from our models and placed 15 stars from Bedding et al. (2020) amongst that distribution (Fig. 11). This indicated that the fundamental mode was misidentified in two of those stars. We also described the utility of the $3\Delta\nu$ approximation for identifying the radial mode (Fig. 10).

We have demonstrated the power of the combining grid with a neural network for parameter inference for δ Sct stars. We revisited HD 139614 and calculated new, more precise stellar parameters from models with a more moderate helium abundance. We performed detailed modelling for three δ Sct stars from Bedding et al. (2020) with measured $v \sin i$, and found them all to be young MS stars with ages < 50 Myr. We also presented two δ Sct stars that have very long radial and dipole ridges comprising a total of 15 and 16 modes for HD 46722 and HD 112063, respectively. We find both of these stars to be in the pre-MS stage, with random uncertainties under 3%. In future work we will incorporate rotation into the models, measure rotationally split modes, and quantify the systematic uncertainties arising from various physical and computational parameters.

ACKNOWLEDGEMENTS

This research made use of Lightkurve, a Python package for Kepler and TESS data analysis (Lightkurve Collaboration et al. 2018). SJM would like to thank Warrick Ball, Guy Davies, Martin Nielsen, and Owen Scutt for discussions during an extended visit to the University of Birmingham, funded by a University of Birmingham Commonwealth Fellowship. SJM was supported by the Australian Research Council (ARC) through Future Fellowship FT210100485. TRB was also supported by the ARC, through DP210103119 and FL220100117.

DATA AVAILABILITY

```
grid_export.csv
grid_export_readme.txt
mesa_inlist
```

REFERENCES

Asplund M., Grevesse N., Sauval A. J., Scott P., 2009, ARA&A, 47, 481
Balona L. A., 2014, MNRAS, 437, 1476
Barac N., Bedding T. R., Murphy S. J., Hey D. R., 2022, MNRAS, 516, 2080
Barceló Forteza S., Roca Cortés T., García R. A., 2018, A&A, 614, A46
Barceló Forteza S., Moya A., Barrado D., Solano E., Martín-Ruiz S., Suárez J. C., García Hernández A., 2020, A&A, 638, A59
Basu S., Hekker S., 2020, Frontiers in Astronomy and Space Sciences, 7, 44
Bedding T. R., et al., 2020, Nature, 581, 147
Bedding T. R., et al., 2023, ApJ, 946, L10
Brogaard K., et al., 2012, A&A, 543, A106
Currie T., et al., 2023, Science, 380, 198
Curtis J. L., Agüeros M. A., Mamajek E. E., Wright J. T., Cummings J. D., 2019, AJ, 158, 77
Dupret M.-A., Grigahcène A., Garrido R., Gabriel M., Scuflaire R., 2004, A&A, 414, L17
Folsom C. P., Bagnulo S., Wade G. A., Alecian E., Landstreet J. D., Marsden S. C., Waite I. A., 2012, MNRAS, 422, 2072
Gagné J., Moranta L., Faherty J. K., Kiman R., Couture D., Larochelle A. R., Popinchalk M., Morrone D., 2023, ApJ, 945, 119
Galindo-Guil F. J., et al., 2022, A&A, 664, A70
Gander M. J., Vandewalle S., 2007, SIAM J. Sci. Comput., 29, 556
García Hernández A., Martín-Ruiz S., Monteiro M. J. P. F. G., Suárez J. C., Reese D. R., Pascual-Granado J., Garrido R., 2015, ApJ, 811, L29
García Hernández A., et al., 2017, MNRAS, 471, L140
Gray R. O., Riggs Q. S., Koen C., Murphy S. J., Newsome I. M., Corbally C. J., Cheng K.-P., Neff J. E., 2017, AJ, 154, 31
Guggenberger E., Hekker S., Basu S., Bellinger E., 2016, MNRAS, 460, 4277
Guzik J. A., Jackiewicz J., Catanzaro G., Soukup M. S., 2021, arXiv e-prints, p. arXiv:2107.09479
Hasanzadeh A., Safari H., Ghasemi H., 2021, MNRAS, 505, 1476
Hawkins K., Lucey M., Curtis J., 2020, MNRAS, 496, 2422
Hekker S., 2020, Frontiers in Astronomy and Space Sciences, 7, 3
Henyey L., Vardya M. S., Bodenheimer P., 1965, ApJ, 142, 841
Jackiewicz J., 2021, Frontiers in Astronomy and Space Sciences, 7, 102
Kama M., Folsom C. P., Pinilla P., 2015, A&A, 582, L10
Kerr R., Kraus A. L., Murphy S. J., Krolikowski D. M., Offner S. S. R., Tofflemire B. M., Rizzuto A. C., 2022a, ApJ, 941, 49
Kerr R., Kraus A. L., Murphy S. J., Krolikowski D. M., Bedding T. R., Rizzuto A. C., 2022b, ApJ, 941, 143
Kiehl M., 1994, Parallel Comput., 20, 275
Kjeldsen H., Bedding T. R., 1995, A&A, 293, 87
Kurtz D. W., 2022, ARA&A, 60, 31
Li T., Bedding T. R., Huber D., Ball W. H., Stello D., Murphy S. J., Bland-Hawthorn J., 2018, MNRAS, 475, 981
Lightkurve Collaboration et al., 2018, Lightkurve: Kepler and TESS time series analysis in Python, Astrophysics Source Code Library (ascl:1812.013)
Linsky J. L., 1998, Space Sci. Rev., 84, 285
Lyttle A. J., et al., 2021, MNRAS, 505, 2427
Mamajek E. E., Meyer M. R., Liebert J., 2002, AJ, 124, 1670
McNamara D., 1997, PASP, 109, 1221
Meingast S., Alves J., Fürnkranz V., 2019, A&A, 622, L13
Miret-Roig N., Galli P. A. B., Olivares J., Bouy H., Alves J., Barrado D., 2022, A&A, 667, A163
Mirouh G. M., Angelou G. C., Reese D. R., Costa G., 2019, MNRAS, 483, L28
Murphy S. J., Paunzen E., Bedding T. R., Walczak P., Huber D., 2020, MNRAS, 495, 1888
Murphy S. J., Joyce M., Bedding T. R., White T. R., Kama M., 2021, MNRAS, 502, 1633
Murphy S. J., Bedding T. R., White T. R., Li Y., Hey D., Reese D., Joyce M., 2022, MNRAS, 511, 5718
Netzel H., Pietrukowicz P., Soszyński I., Wrona M., 2022, MNRAS, 510, 1748
Paunzen E., Skarka M., Walczak P., Holdsworth D. L., Smalley B., West R. G., Janík J., 2015, MNRAS, 453, 1241
Paxton B., Bildsten L., Dotter A., Herwig F., Lesaffre P., Timmes F., 2011, ApJS, 192, 3
Paxton B., et al., 2013, ApJS, 208, 4
Paxton B., et al., 2015, ApJS, 220, 15
Paxton B., et al., 2018, ApJS, 234, 34
Paxton B., et al., 2019, ApJS, 243, 10
Pecaut M. J., Mamajek E. E., 2016, MNRAS, 461, 794
Pedersen M. G., Aerts C., Pápics P. I., Rogers T. M., 2018, A&A, 614, A128
Pedersen M. G., et al., 2021, Nature Astronomy, 5, 715
Petersen J. O., Christensen-Dalsgaard J., 1996, A&A, 312, 463
Pinsonneault M. H., et al., 2018, ApJS, 239, 32
Preibisch T., Mamajek E., 2008, The Nearest OB Association: Scorpius-Centaurus (Sco OB2). Astronomical Society of the Pacific Monograph Publications, p. 235
Reese D., Lignières F., Rieutord M., 2008, A&A, 481, 449
Rodrigues T. S., et al., 2017, MNRAS, 467, 1433
Röser S., Schilbach E., 2020, A&A, 638, A9
Scutt O. J., Murphy S. J., Nielsen M. B., Davies G. R., Bedding T. R., Lyttle A. J., 2023, arXiv e-prints, submitted to MNRAS, p. arXiv:2302.11025
Serenelli A., Weiss A., Cassisi S., Salaris M., Pietrinferni A., 2017, A&A, 606, A33
Serenelli A., et al., 2021, A&ARv, 29, 4
Sharma S., Stello D., Bland-Hawthorn J., Huber D., Bedding T. R., 2016, ApJ, 822, 15
Squicciarini V., Gratton R., Bonavita M., Mesa D., 2021, MNRAS, 507, 1381
Stahler S. W., Shu F. H., Taam R. E., 1980, ApJ, 241, 637
Stassun K. G., et al., 2019, AJ, 158, 138
Steindl T., Zwintz K., Barnes T. G., Müllner M., Vorobyov E. I., 2021, A&A, 654, A36
Steindl T., Zwintz K., Müllner M., 2022, A&A, 664, A32
Suárez J. C., Garrido R., Goupil M. J., 2006, A&A, 447, 649
Suárez J. C., García Hernández A., Moya A., Rodrigo C., Solano E., Garrido R., Rodón J. R., 2014, A&A, 563, A7
Townsend R. H. D., 2020, website, Oscillation Parameters, `https://gyre.readthedocs.io/en/latest/ref-guide/input-files/osc-params.html`. `https://gyre.readthedocs.io/en/latest/ref-guide/input-files/osc-params.html`
Townsend R. H. D., Teitler S. A., 2013, MNRAS, 435, 3406
Ulrich R. K., 1986, ApJ, 306, L37
Verma K., Raodeo K., Basu S., Silva Aguirre V., Mazumdar A., Mosumgaard J. R., Lund M. N., Ranadive P., 2019, MNRAS, 483, 4678
White T. R., Bedding T. R., Stello D., Christensen-Dalsgaard J., Huber D., Kjeldsen H., 2011, ApJ, 743, 161

Wood M. L., et al., 2023, AJ, 165, 85
Ziaali E., Bedding T. R., Murphy S. J., Van Reeth T., Hey D. R., 2019, MNRAS, 486, 4348
Zwintz K., et al., 2014, Science, 345, 550
Žerjal M., Ireland M. J., Crundall T. D., Krumholz M. R., Rains A. D., 2023, MNRAS, 519, 3992

APPENDIX A: ADDITIONAL FIGURES FOR THE FIVE NEWLY MODELLED STARS

In this appendix we provide the corner plots for the five modelled stars (refer to Sec. 4) and the corresponding échelle diagrams with posterior-predicted mode frequencies.

This paper has been typeset from a TEX/LATEX file prepared by the author.

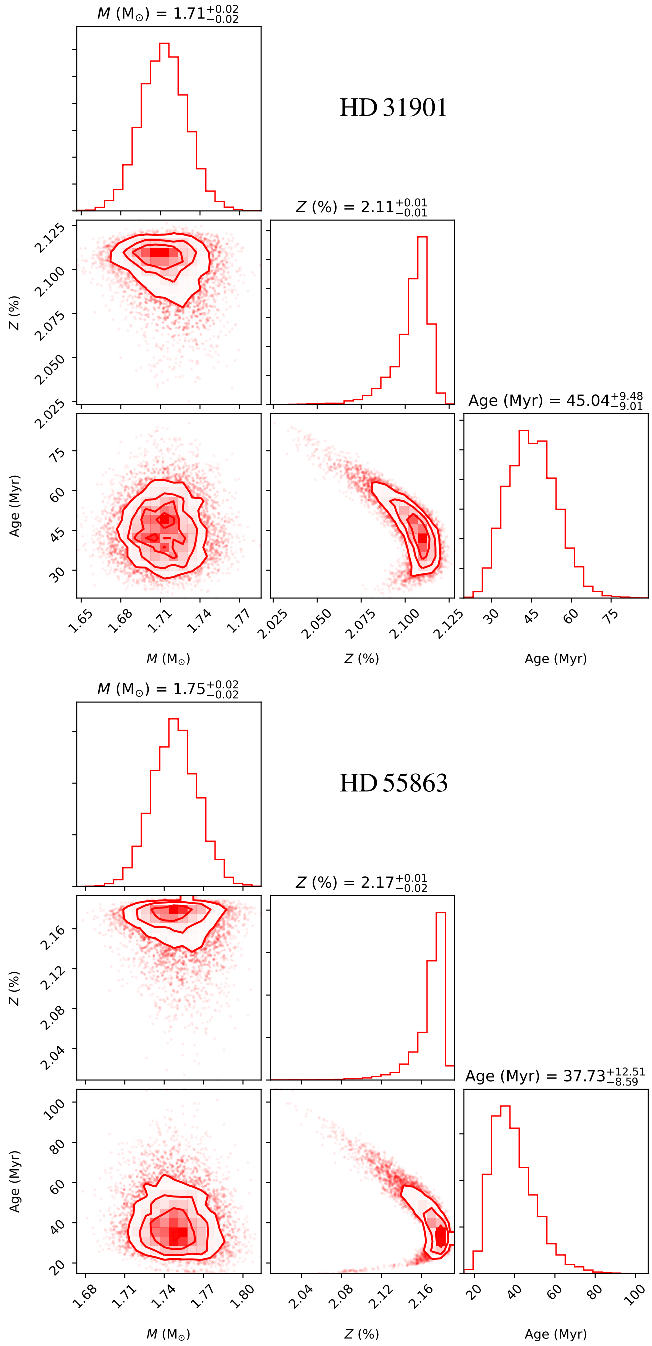

Figure A1. Corner plots for the analysis of two of the three remodelled stars from Bedding et al. (2020): HD 31901 ($33 \pm 4\,\mathrm{km\,s^{-1}}$; top), HD 55863 ($v \sin i = 99 \pm 5\,\mathrm{km\,s^{-1}}$; bottom).

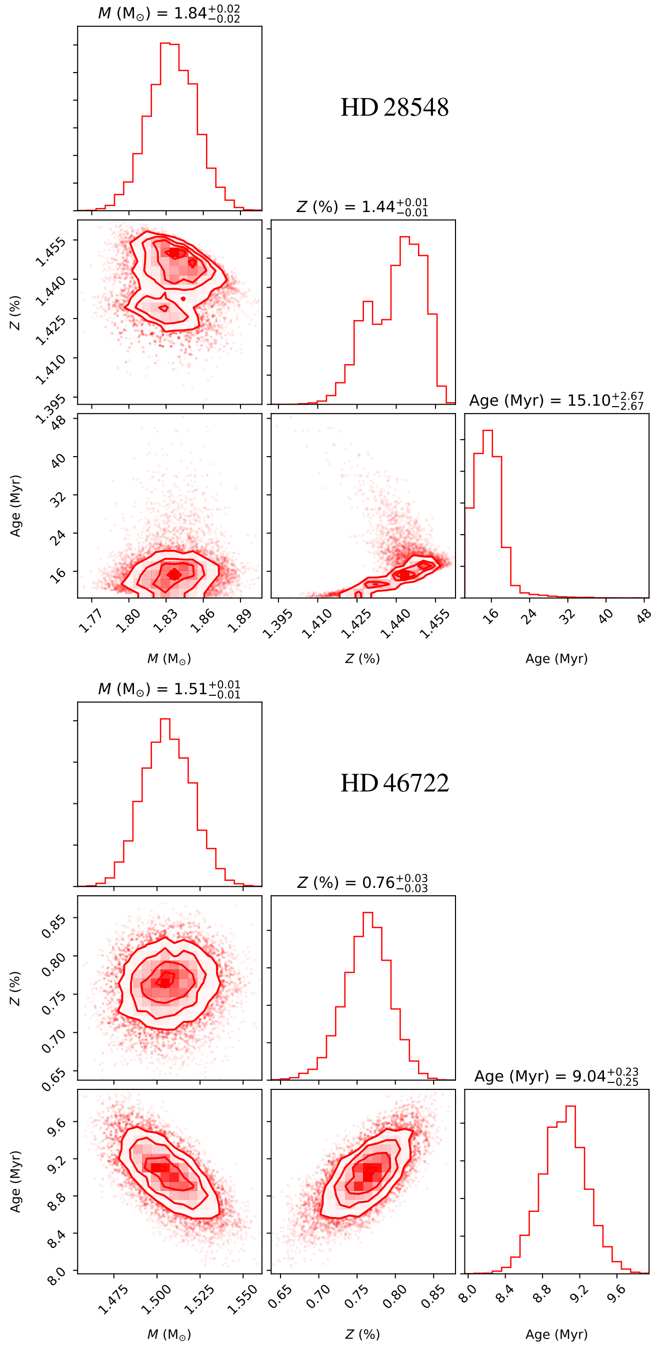

Figure A2. Corner plot for HD 28548 ($v \sin i$ = 200 ± 50 km s^{-1}; top), and for HD 46722 (bottom).

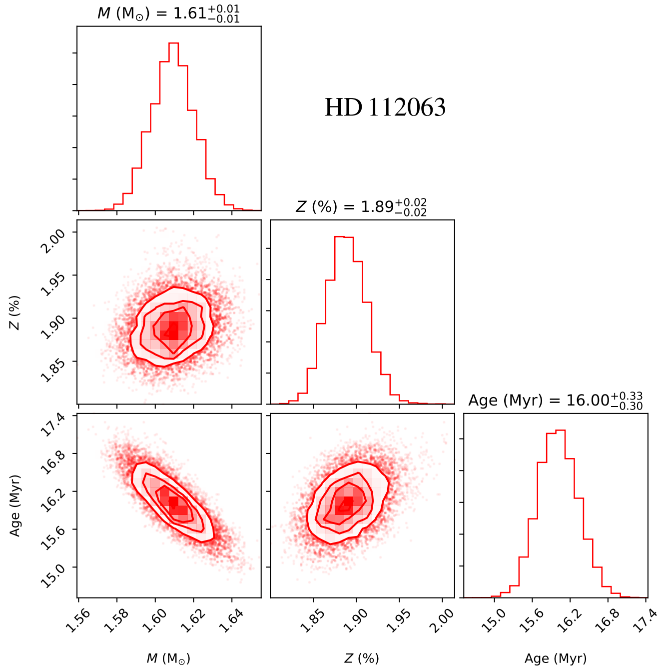

Figure A3. Corner plot for HD 112063.

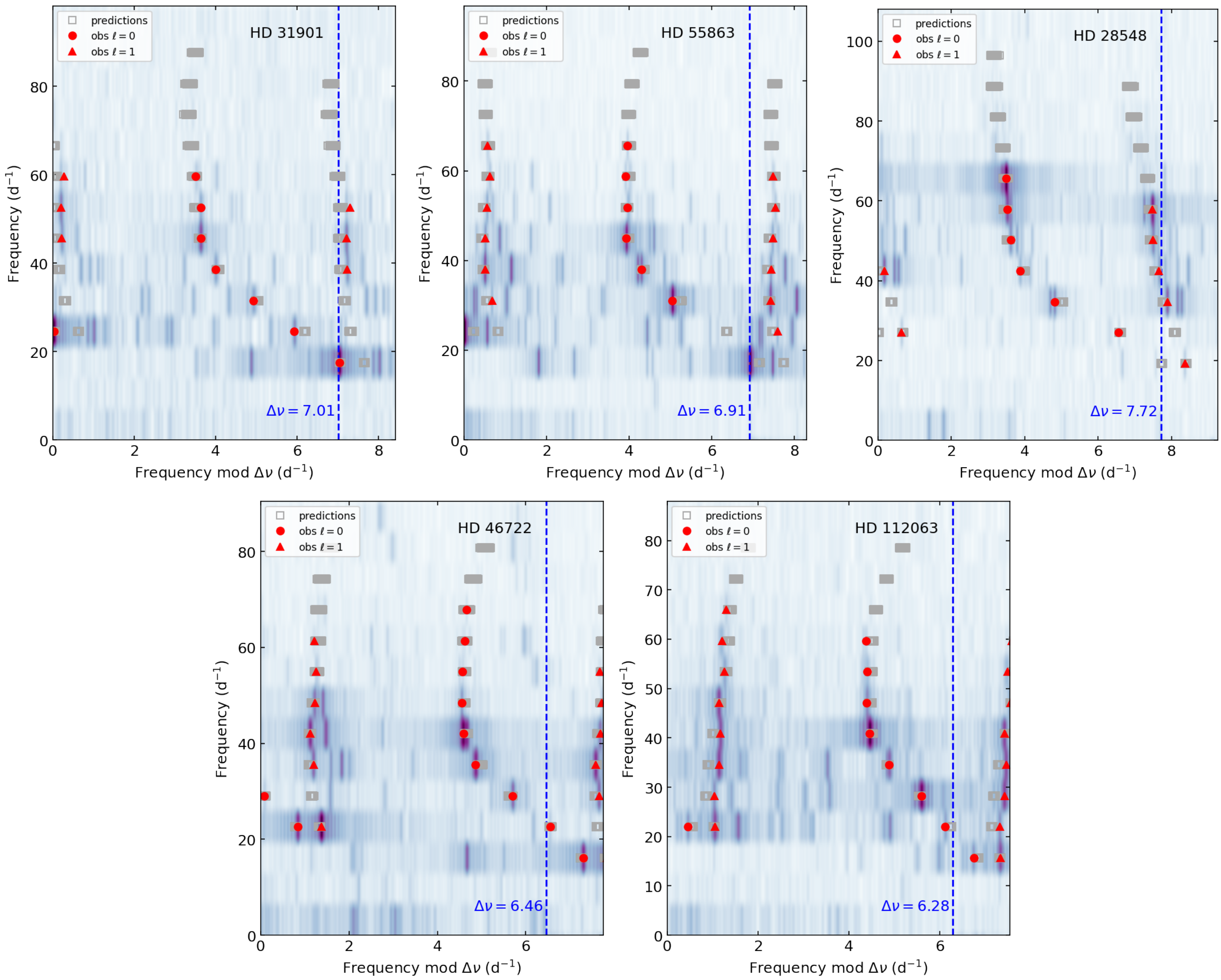

Figure A4. Échelle diagrams of five δ Sct stars. The grey-scale shows the observed amplitude spectra; the red points mark the identified modes, and the grey squares show posterior-predicted mode frequencies from the neural network.